Finite Element Simulation on the Interface Bonding Performance of Microrockbolt-Grouting Body

Ye Liang[1] , Huang Zhiqiang[1], Liu Yang[2,*], Ye Chengze[3] and Wu Zhenlei[4]

[1]*School of Civil Engineering and Architecture, Zhejiang University of Science and Technology, Hangzhou 310023, China*
[2]*Business School, Shanghai Jian Qiao University, Shanghai 201306, China*
[3]*International Campus, Zhejiang University, Haining 314499, China*
[4]*Longyou County Museum, Longyou 324400, China*

_____

Abstract

China's grotto temples have suffered from the erosion caused by shallow-surface peeling diseases for many years, and the common protection technology cannot solve such problems. Therefore, in view of the characteristics of wide distribution, small rock separation parts, and shallow layers of spalling diseases in cave temples, the microrockbolt anchoring technology was adopted for treatment. On the basis of the finite element method, the pulling process of microrockbolt–grouting body was simulated, the interface bonding mechanical property between microrockbolt and grouting materials was explored, and the influence of different rockbolt diameters and anchorage lengths on the microrockbolt pulling force was analyzed under monotonic load. Results show that all the failure forms are bolt pulling out failure. With the increase in anchorage length and reinforcement diameter, the axial stress in the anchoring section decreases gradually, and the stress decreases almost uniformly along the anchorage length. The increase in steel bar diameter causes the ultimate pulling force of microbolt to increase. With the increasing of anchorage length, the ultimate pulling force of microbolt increases, but the increase rate decreases. The average interface bond strength decreases when the anchorage length is 100-250 mm. The conclusions obtained in this study provide a significantly reference for the microrockbolt anchoring treatment in cave temples with shallow-surface spalling diseases.

Keywords: Cave temples with spalling disease, Microrockbolt pulling force, Finite element analysis, Interface bonding performance
_____

1. Introduction

There were a total of 308 rock caves and stone carving relics are under national key protection in China in 2022 [1]. With the passage of time, increasing stone cultural relics have been damaged to varying degrees because of such factors as natural disasters, biological disasters, meteorological disasters, and man-made damage. Damaged rocks mainly have the characteristics of surface weathering, mechanical damage, and part shedding [2].

It is not difficult to see from the development process of the protection and reinforcement technology of the cliff body of the cave temple and the cave rock mass, the progress of technology is closely related to the development of the concept. The protection of the grottoes excavated on the sand conglomerate has developed from the initial retaining wall-roof support to the more concealed anchorage technology, local roof support technology, crack grouting technology, surface anti-weathering technology, etc. The whole process fully reflects the concepts and principles of minimum intervention, maximum compatibility, moderate protection. It played an important role in the rescue and reinforcement period of the cliff body of the cave temple and the cave rock mass. With the elimination of major dangers, the grottoes have entered the stage of scientific protection. At present, the concept of preventive protection has been paid attention to in the important grottoes, and the construction of corresponding monitoring and early warning

system have laid the foundation for preventive protection in the later stage.

A relatively mature theoretical system has been formed for the anchor (cable) technology used in the collapse of large-volume dangerous rocks. However, the spalling disease of caves and cave temples has the characteristics of small volume, wide distribution, and small separation of stone and shallow layers. Moreover, owing to the unique nature of cultural relics, adopting restoration methods that will cause greater damage is impossible. Therefore, the use of microrockbolt to treat this disease is a reasonable choice [3-5].

In this study, the finite element software ABAQUS was used to model grouting body and microrockbolt. The influences of different bolt diameters and anchorage lengths on the pulling force and axial normal stress distribution of microrockbolt under the action of monotone load were simulated and analyzed. The anchoring effect of microrockbolt on the shallow-surface spalling disease of cave temples was discussed.

2. State of the Art

In terms of the categories and types of diseases, many scholars have put forward considerable opinions. Li [6] systematically studied the classification of deterioration forms in the field of deterioration investigation of cultural relic rock materials in the world and proposed a three-level classification structure combined with domestic and foreign

research. Yu et al. [7] evaluated 38 grotto temples and time-type cultural relics in Zhejiang Province and found that the top three diseases of stone cultural relics in Zhejiang were surface layer weathering, biological diseases, and water seepage. Huang et al. [8] studied the disease mechanism of sandstone grottoes by focusing on the key technologies for the treatment of dangerous rock mass in sandstone grottoes. Wang et al. [9-11] described the characteristics of China's grotto temples, summarized the basic process of the protection of grotto temples, and analyzed the main problems existing in China's grotto temples. In 2021, combined with the climate environment and the disease situation of stone cultural relics, the disease of stone cultural relics was classified into 8 categories and 22 subcategories. In 2022, from the two dimensions of grottoes' environment and cultural relics, the damage effects of grottoes' diseases were classified, and the concept and types of such diseases were analyzed.

In view of the drawing process of rock and bolt, some scholars also put forward the numerical simulation method to study and achieved certain results [12-14]. Fu et al. [15] obtained the stress and deformation characteristics of prestressed rockbolt wind turbine foundation under external load through FLAC3D numerical simulation analysis and studied the influence of changes in bolt length and diameter on wind turbine foundation. Giot et al. [6] measured the axial strain of the bolt from its head to the far end through in situ pullout test, and the results showed that the bonding effect between the rod and the grouting body was better than the far end of the rod body. Vlachopoulos et al. [17] carried out numerical modeling of pullout test, conducted a laboratory pullout test, compared experimental and modeling results, and evaluated the feasibility of the numerical method and its corresponding relationship with the experiment. Komurlu and Demir [18] studied core drilling specimens, evaluated their usability in determining the direct tensile strength of rock materials, and discussed the test method and its failure mechanism. Kou et al. [19] conducted segmental modeling of anchor rod and cement mortar, studied the bolt–mortar interface slip curve, and analyzed and compared it with field test results. Dimitrienko et al. [20] developed an effective numerical solution method for stress–strain state considering block curve anisotropy and creep based on the modeling of rock's stress–strain state. Abdel-Rahman and Awad-Allah [21] verified the feasibility of the three-dimensional finite element method and empirical method in predicting the pulling resistance (skin friction) of ground anchors in soil and studying soft rock formation. Małkowski et al. [22] studied the bonding properties of rockbolts under three different grouting materials by laboratory tests and numerical simulation.

Many scholars have explored the model of two interfaces in rock, bolt, and grout and obtained some theoretical models by fitting the data of laboratory drawing test with numerous calculations. Liu and Li [23] based on the hyperbolic model established by interface spring theory and carried out fitting analysis on the measured test data. Liu et al. [24] established a mathematical model that can describe the three stages of elastic state, plastic softening, and cracking and sliding of the bolt–mortar interface when a long bolt was subjected to uplift load. Tan et al. [25] carried out a theoretical analysis on the bond slip behavior of the interface between bolt and grout and verified the correctness of its derivation through the data curve rule of drawing test. Zhao et al. [26] conducted a comparative evaluation of four concrete models through test data and found that the new concrete damage plastic model provided the most accurate simulation of the cyclic behavior of concrete. Li et al. [27] verified the rationality of the simplified bilinear model through experiments and numerical simulation and derived the expressions of interfacial bond stress. Kong et al. [28] derived the difference scheme of the governing equation of the full-length bonded bolt body–mortar interface based on the three-broken line bond slip model. Tamiru et al. [29] carried out progressive failure analysis of composite pipes and achieved good results. Abbas et al. [30] realized good results by combining the modified cohesion model (CZM) based on the Tvergaard method and the friction model of the damaged site of the interface to consider friction and damage between steel bars and concrete.

To explore the application of microbolt in the protection of stone cultural relics from spalling disease, two interfaces of rock, grout, and microbolt are called the first and second interface. The first interface is the face between microbolt and grout, and the second interface is the interface between rock and grout. With the first interface (the interface between microbolt and grout) as the starting point, on the stress distribution and ultimate pulling force on the bolt are studied by numerical simulation calculation method, and the relationship between ultimate pulling force and interface bonding strength is determined.

The rest of this study is organized as follows. Section 3 introduces the numerical simulation process. Section 4 mainly analyzes the results and discusses the influences of bolt diameter and anchorage length on the stress distribution and ultimate pulling force on the bolt via a single-factor control method. Finally, the conclusions are summarized in Section 5.

3. Methodology

3.1 Finite element model
This chapter mainly simulates the extraction process of microbolt and grout material by numerical simulation. The influences of different anchorage lengths and steel bar diameters on stress distribution and ultimate pulling force and the relationship between ultimate pulling force and interface bonding strength are analyzed. The effects of different factors on the uplift bearing capacity of microbolt and grouting material are also studied.

3.2 Mechanical properties of materials
A cement mortar with a strength grade of M30 is selected for grout. The relevant mechanical parameters are shown in Table 1.

Table 1. Material parameters of the grouting body.

Density (kg·m⁻³)	Elastic modulus (GPa)	Poisson's ratio
2450	48	0.20

The rockbolts are made of HRB335 steel bars, and an elastic constitutive relationship is adopted. The material parameters are shown in Table 2.

Table 2. Material parameters of the HRB335 steel bar.

Density (kg·m⁻³)	Elastic modulus (GPa)	Poisson's ratio
7890	206	0.30

3.3 Cohesive zone model
The commonly used interface models between grout and bolt in the academic community include interface spring analysis model, bilinear bond–slip model, and simplified

bilinear bond–slip model [23, 25, 27]. A bilinear bond–slip constitutive relationship (traction–separation laws) is applied to the interface model between the grouting body and the microrockbolt in this study [16], as shown in Fig. 1.

This model is divided into ascending and descending segments, both of which are linear. The vertex of the ascending segment is the maximum stress, while the stress in the descending segment gradually decreases. When the stress decreases to 0, the interface is damaged and fails.
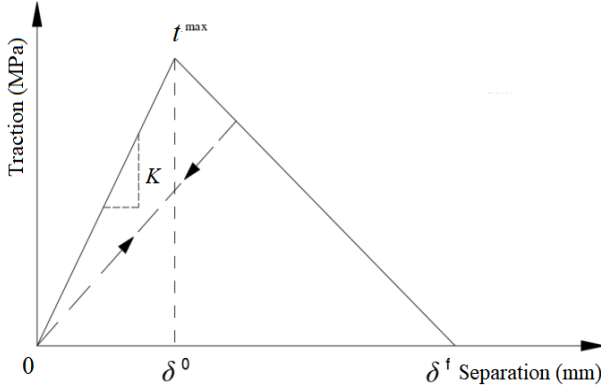

Fig. 1. Bilinear bond–slip constitutive model

The ascending segment shown in Fig. 1 is an elastic behavior; t represents the traction stress, δ^0 represents the initial displacement of damage, and δ_f represents the termination displacement of damage. The specific formulas are as follows:

$$t = \begin{Bmatrix} t_1 \\ t_1 \\ t_1 \end{Bmatrix} = \begin{bmatrix} K_{11} & K_{12} & K_{13} \\ K_{21} & K_{22} & K_{23} \\ K_{31} & K_{32} & K_{33} \end{bmatrix} \begin{Bmatrix} \delta_1 \\ \delta_2 \\ \delta_3 \end{Bmatrix} = K\delta \tag{1}$$

In the three-dimensional problem, t_1, t_2, t_3 are the traction stresses in three directions, and δ_1, δ_2, δ_3 represent the separation displacements in three directions. The common criterion for the initial damage of cohesive behavior is the maximum stress criterion. When damage occurs, the ratio between each contact stress and the maximum contact stress in the three directions is greater than 1, that is, the maximum contact stress ratio is greater than 1. When the interface is not damaged, the ratio between the contact stress in the three directions and the maximum contact stress is less than 1. The maximum stress criterion formula [31] is:

$$\max \left\{ \frac{t_1}{t_1^{max}}, \frac{t_2}{t_2^{max}}, \frac{t_3}{t_3^{max}} \right\} = 1 \tag{2}$$

The descending stage is the damage evolution process, which begins to evolve when the damage initiation criterion is reached. The formulas are as follows:

$$t_1 = \begin{cases} (1 - D)\overline{t_1} & \overline{t_1} \geq 0 \\ \overline{t_1} & \text{otherwise no damage} \end{cases} \tag{3}$$

$$t_2 = (1 - D)\overline{t_2} \tag{4}$$

$$t_3 = (1 - D)\overline{t_3} \tag{5}$$

where respectively represent the components of contact stress predicted by elastic traction-separation without considering damage. The linear damage evolution coefficient D is 0 when the damage starts and increases monotonically from 0 to 1 during the damage process, it can be expressed as

$$D = \frac{\delta_m^f \left(\delta_m^{max} - \delta_m^0 \right)}{\delta_m^{max} \left(\delta_m^f - \delta_m^0 \right)} \tag{6}$$

where the lower corner mark m of δ in the formula represents the effective displacement determined using Eq. (5), and δ_m^{max} refers to the maximum effective separation achieved during the loading process.

$$\delta_m = \sqrt{\delta_1^2 + \delta_2^2 + \delta_3^2} \tag{7}$$

The considerable calculations in the early stage reveal that the cohesive force model is easy to converge.

After the general setting of the interface, the relevant parameters of cohesion force are set, and the interface stiffness is set in terms of bond behavior. The empirical value range of tangential bond slip stiffness K of the contact surface is 5.0-13.5 MPa/mm; for conservative reasons, 5.0 MPa/mm is considered. Given that the normal direction defines hard contact, the stiffness here is regarded as 0 [32]. The damage setting is divided into two modules: damage initiation and damage evolution. The maximum stress criterion is used for damage initiation, and the traction stress in all three directions needs to be input as 1 MPa. The total/plastic displacement in the failure displacement is 0.1, which is derived from the time of damage initiation (The displacement experienced from the peak traction stress to 0).

3.4 Model establishment
The grout and microbolt are modeled. The grout size is designed in accordance with the size of the conventional pouring mold. The grouting body is a cuboid of 100 × 100 × 150 mm, with a perforating cavity , and the bolt is a cylinder with a height of 300 mm. The diagram of the microanchor rod is shown in Fig. 2.
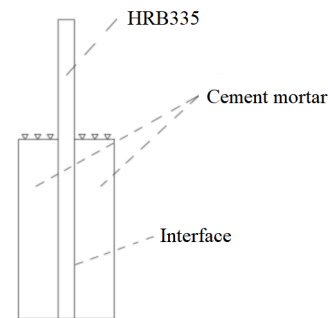

Fig. 2. Schematic of microrockbolt pulling.

The model is based on commonly used steel bar diameters, and the interface section between the anchor rod and the grouting body is partitioned. The modeling is shown in Fig. 3.
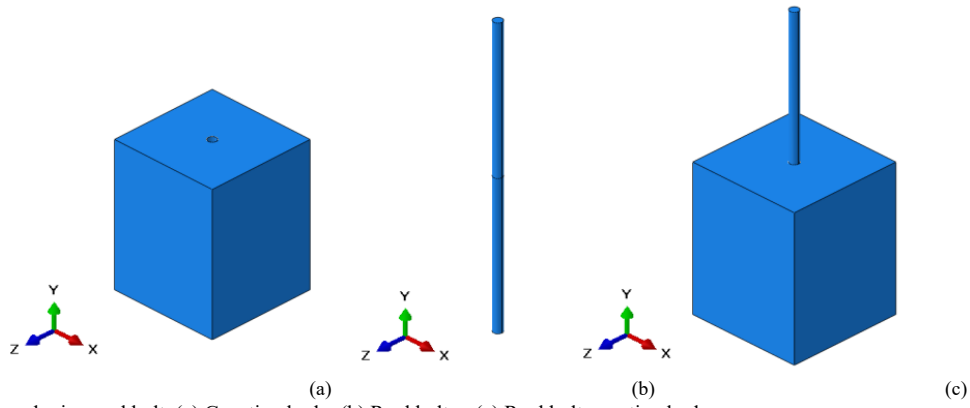
(a) (b) (c)

Fig. 3. Grouting body and microrockbolt. (a) Grouting body. (b) Rockbolt. (c) Rockbolt-grouting body.
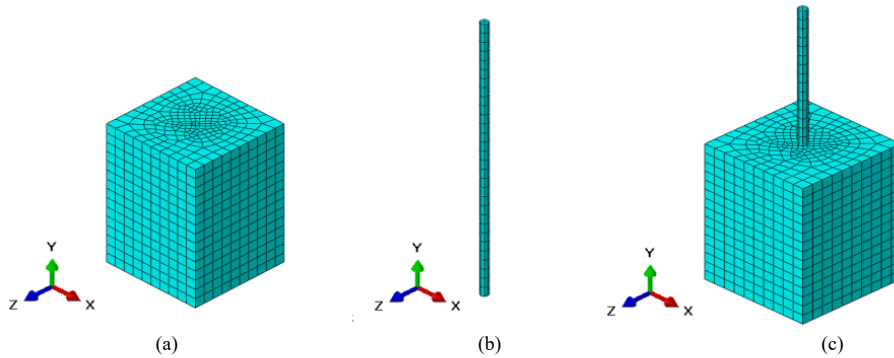

(a) (b) (c)

Fig. 4. Mesh of grouting body and micro-rockbolt. (a) Grouting body. (b) Rockbolt. (c) Rockbolt-grouting body.

3.5 Boundary conditions and loads
With reference to the actual experimental process, the upper end face of the grouting body in the finite element model is fixed and constrained in the simulation. The top surface of the anchor rod is coupled with reference points, and the displacement control method is used to apply force along the length direction of the anchor rod and pullout 1 mm along the reference point. The specific setting of boundary conditions is shown in Fig. 5.
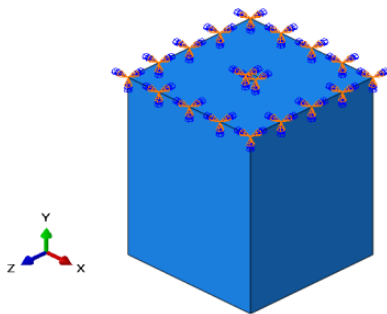

Fig. 5. Setting of boundary conditions.

3.6 Contact setting
In addition to the cohesion model mentioned above, a conventional contact setting demonstrating the friction between different entities, which is represented as a mechanical bite force when the cohesion model reaches the damage termination displacement, should also be established. The general contact is used to set the contact properties after the failure of interface bonding force. The contact properties of the whole model are assigned to two directions, namely, normal and tangential contact properties.

4. Result analysis and discussion

4.1 Effect of anchorage length on stress distribution
A steel bar diameter of 10 mm is selected, and a monotonic load of 3 kN is applied along the axial direction of the anchor rod to the reference point set on the top end face of the anchor rod. The axial normal stress distribution of the anchor rod (The anchorage length is 100, 150, 200, and 250 mm, respectively) is simulated and calculated, as shown in Fig. 6.

According to the finite element calculation (Table 3), the maximum principal stress on the bolt is along the bolt direction. When the load reaches 3 kN, the stress cloud map shows that the maximum stress in the whole bolt does not reach the set failure tensile stress value. When the conditions are determined by other factors, under the four anchorage lengths, the maximum stress, which is 42.43 MPa, occurs at the loading end of the bolt.
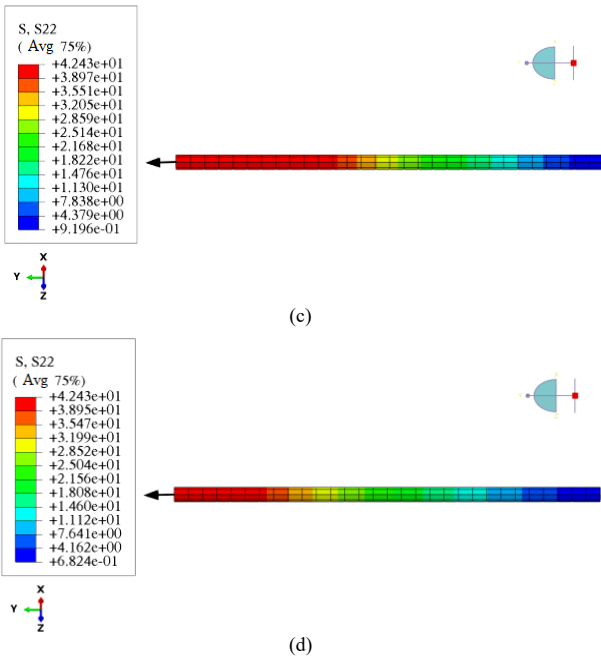

(a)

(b)

(c)

(d)
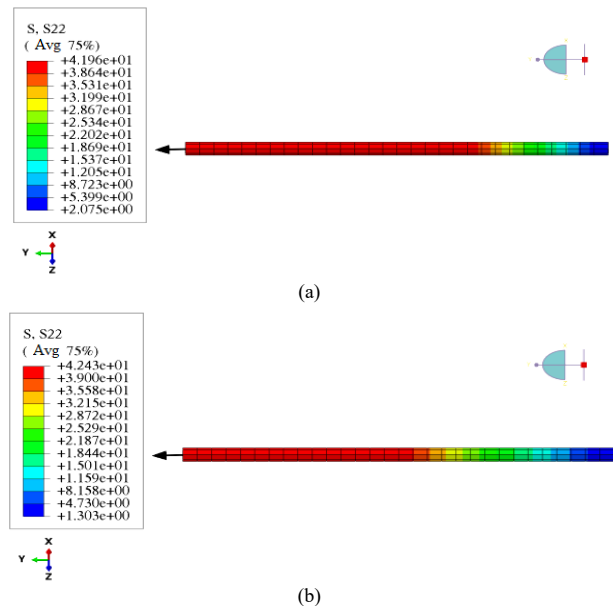
Fig. 6. Axial stress cloud diagram of microrockbolt with different anchorage lengths. (a) 100 mm. (b) 150 mm. (c) 200 mm. (d) 250 mm.

As seen from Fig. 7, the stress distribution of the microrockbolt under different anchorage lengths follows the pattern below: when the anchorage length is 100, 150, 200, and 250 mm, the maximum principal stress is located at the starting position of the anchoring section, and the stress values are 40.856, 41.539, 41.741, and 41.700 MPa, respectively. Within a certain range of anchorage length, that is, from 100 mm to 200 mm, the stress rises from 40.856 MPa to 41.539 MPa and then to 41.741 MPa, and the stress changes are 0.683 and 0.202 MPa, respectively, because the interface between the bolt and the grout has a constraint effect. If the applied load remains unchanged, the stress should be increasing when the anchorage length is 100-200 mm. At 250 mm, the stress drops from 41.741 MPa to 41.700 MPa, which is 0.041 MPa lower than that at 200 mm. The reason is that the increase in anchorage length makes the section exceed the constraint effect. Under the same load, the stress distribution of the 250 mm anchor rod is more uniform, which plays a role in reducing pressure to a certain extent. With the increase in anchorage length, the axial stress distribution in the anchoring section decreases gradually, and the stress value decreases almost uniformly. The stress changes are similar in the four cases.
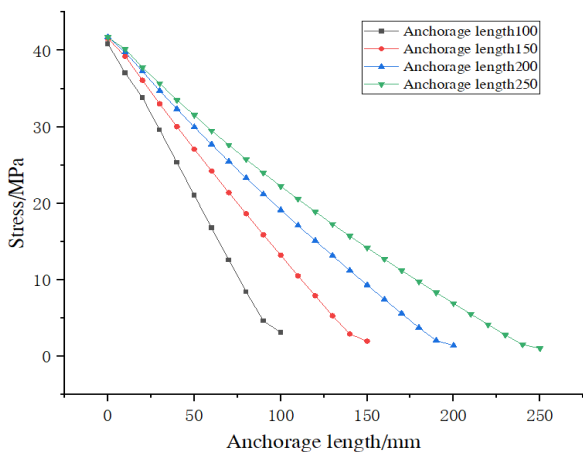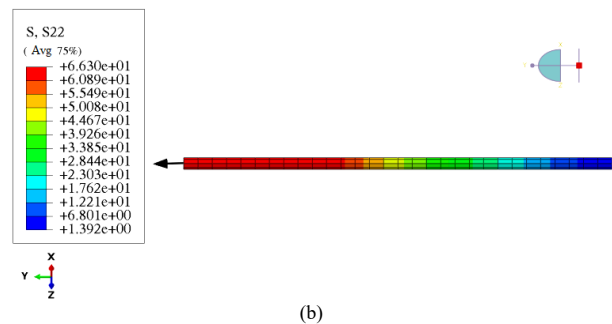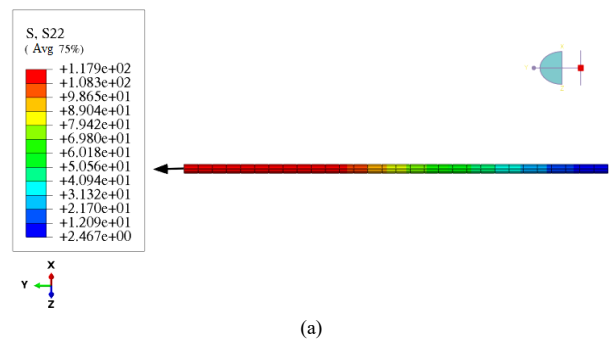

Fig. 7. Axial stress cloud diagram of the microrockbolt with different anchorage lengths.

4.2 Influence of rockbolt diameter on stress distribution
To study the effect of anchor rod diameter on stress distribution, an anchor length of 200 mm is selected. A monotonic load of 3 kN is applied to the reference point set on the top end face of the anchor rod in the positive direction of the y-axis. The stress distribution of the anchor rod is simulated and calculated for steel bars with diameters of 6, 8, and 10 mm. The results are shown in Fig. 8.

Table 3. Simulation results of axial stress distribution with different anchorage lengths under a reinforcement diameter of 10 mm.

| Axial length (mm)	Axial stress (MPa)			
	Anchorage length 100 mm	Anchorage length 150 mm	Anchorage length 200 mm	Anchorage length 250 mm
0	40.8564	41.5388	41.741	41.7002
10	37.0374	39.2284	39.7634	40.1758
20	33.8076	36.0848	37.2581	37.7666
30	29.6109	33.0062	34.7118	35.6932
40	25.319	30.0213	32.3366	33.4824
50	21.0468	27.0736	29.959	31.5241
60	16.7713	24.22	27.7006	29.487
70	12.5849	21.3795	25.4651	27.6331
80	8.42624	18.6297	23.3078	25.7445
90	4.62697	15.8738	21.1902	23.9849
100	3.1033	13.2026	19.1191	22.2224
110	--	10.5108	17.0975	20.5469
120	--	7.89622	15.0978	18.8903
130	--	5.27977	13.1522	17.2886
140	--	2.90188	11.2095	15.7197
150	--	1.9559	9.32153	14.1815
160	--	--	7.42248	12.684
170	--	--	5.57613	11.1986
180	--	--	3.73087	9.75734
190	--	--	2.05863	8.31436
200	--	--	1.37712	6.9155
210	--	--	--	5.50509
220	--	--	--	4.13659
230	--	--	--	2.76643
240	--	--	--	1.52731
250	--	--	--	1.02061

(a)

(b)

(c)
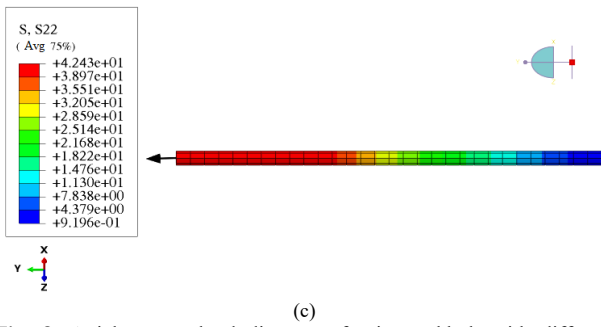
Fig. 8. Axial stress cloud diagram of microrockbolt with different anchorage lengths. (a) 6 mm. (b) 8 mm. (c) 10 mm.

As seen from Fig. 9, when the anchoring depth is 200 mm, the stress distribution of different anchor rod diameters has the following pattern:
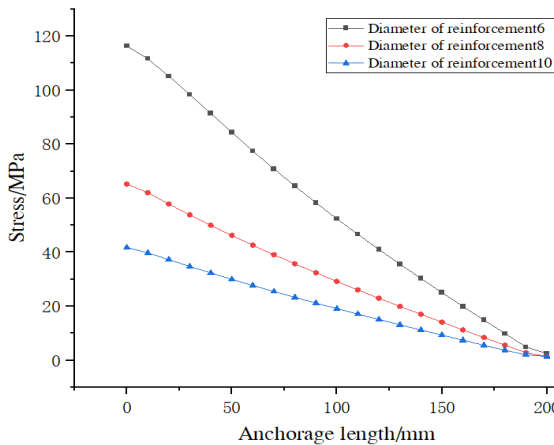

Fig. 9. Axial stress cloud diagram of microrockbolt with different anchorage lengths

In Table 4, the initial stress on the anchorage section decreases. When the diameter of reinforcement bars is 6, 8, and 10 mm, the maximum principal stress is located at the junction between the anchorage section and the uppermost surface of the grouting body, and the stress values are 116.345, 65.217, and 41.741 MPa, respectively. The diameter of the anchor rod ranges from 6 mm to 10 mm. The maximum principal stress changes are 51.128 and 23.476 MPa. The maximum principal stress in the anchoring section increases with the decrease in the bolt diameter within a certain range, that is, when the bolt diameter is 6-10 mm, and the stress changes are obvious. With the increase in the bolt diameter, the maximum principal stress decreases slowly. The stress distribution diagram along the rod direction is also gentle, and the stress distribution of 10 mm bolt is uniform under the same load action and anchorage length. With the increase in reinforcement diameter, the stress of the anchorage section decreases gradually, and the stress decreases almost uniformly along the direction of anchorage length.

Table 4. Simulation results of axial stress distribution under different rockbolt diameters with an anchorage length of 200 mm.

Axial length (mm)	Axial stress (MPa)		
	Rockbolt diameter 6 mm	Rockbolt diameter 8 mm	Rockbolt diameter 10 mm
0	116.345	65.2167	41.741
10	111.617	62.0052	39.7634
20	105.126	57.8324	37.2581
30	98.3707	53.8128	34.7118
40	91.3864	49.9387	32.3366
50	84.3421	46.199	29.959
60	77.4571	42.5837	27.7006
70	70.8317	39.0825	25.4651
80	64.4578	35.6863	23.3078
90	58.3121	32.3854	21.1902
100	52.3732	29.1714	19.1191
110	46.6196	26.0353	17.0975
120	41.0315	22.969	15.0978
130	35.5884	19.9639	13.1522
140	30.2718	17.0127	11.2095
150	25.0625	14.1069	9.32153
160	19.9424	11.2393	7.42248
170	14.8933	8.40217	5.57613
180	9.89801	5.58812	3.73087
190	4.93908	2.78992	2.05863
200	2.46825	1.39408	1.37712

4.3 Relationship between ultimate pullout force and anchorage length

For the anchor length of 100, 150, 200, and 250 mm, the load and displacement for four different anchor lengths with steel bar diameter of 6, 8, and 10 mm are shown below. With the influence of anchorage length considered, the simulation results of the ultimate tensile force changing with the anchorage length are shown in Table 5.

Table 5. Simulation results with the influence of anchorage length considered.

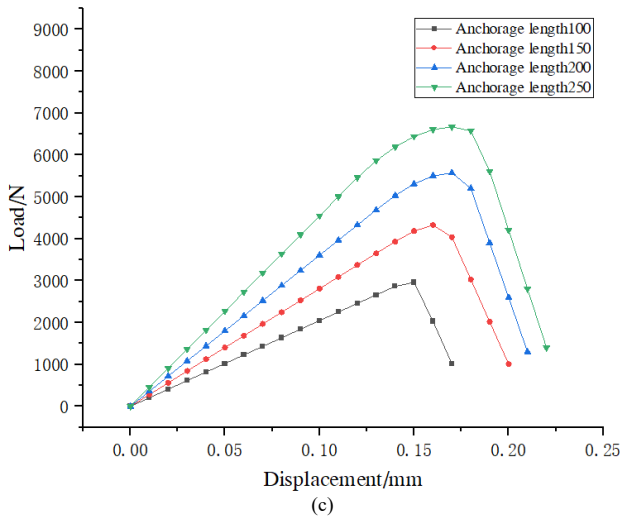| Anchorage length (mm)	Ultimate pullout force (N)		
	Steel bar diameter 6 mm	Steel bar diameter 8 mm	Steel bar diameter 10 mm
100	1757.61	2362.07	2957.22
150	2535.78	3434.44	4328.66
200	3204.05	4376.19	5571.91
250	3759.93	5206.76	6670.00

(a)

(b)
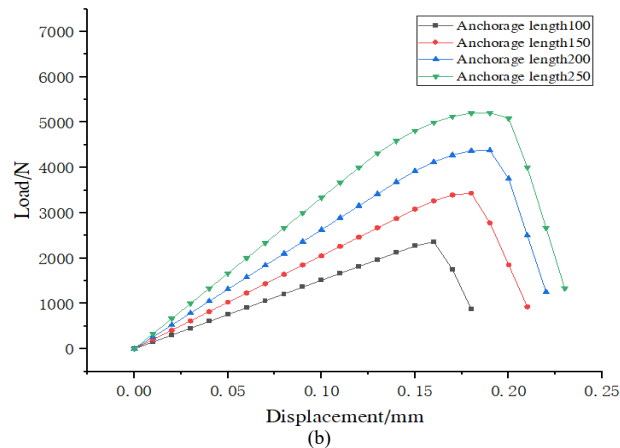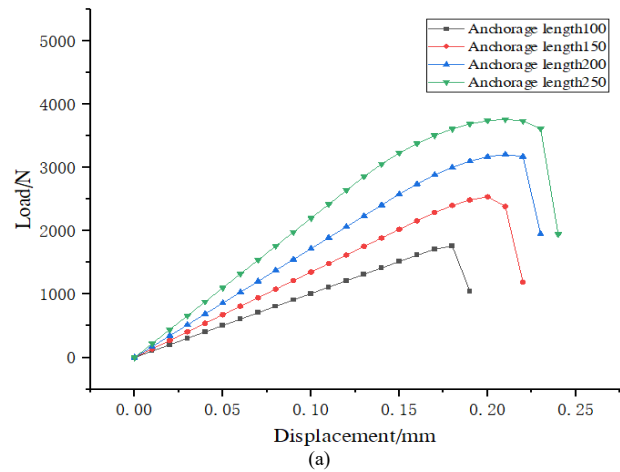
Fig. 10. Load–displacement diagram of different rockbolt diameters. (a) 6 mm. (b) 8 mm. (c) 10 mm.

When the diameter of the steel bar is 6, 8, and 10 mm, the drawing force changes with the anchorage length, as shown in Fig. 11. From the trend of the three pullout force–displacement diagrams, the larger the anchorage length, the greater the pulling force borne by the microanchor rod, and the greater the pulling displacement required to achieve the maximum stress. After the maximum pulling force is reached, the pulling force begins to drop abruptly in a very short time, then the interface bonding fails completely.
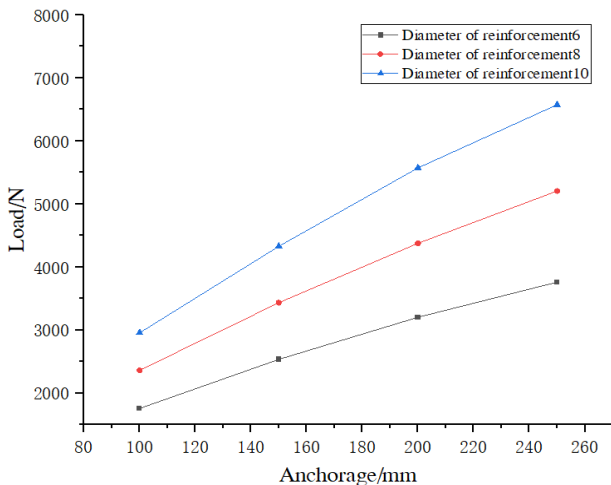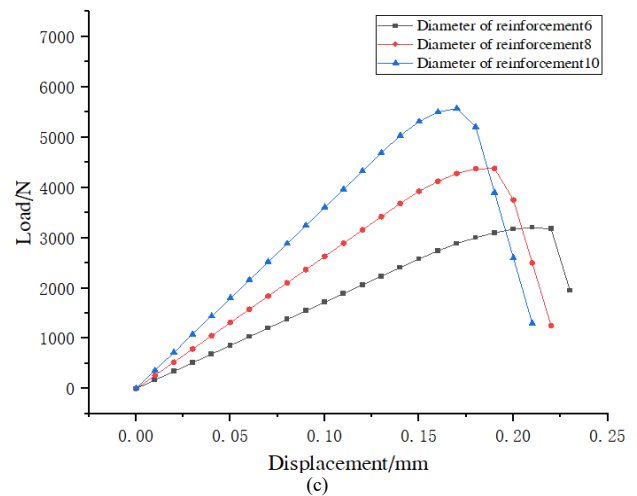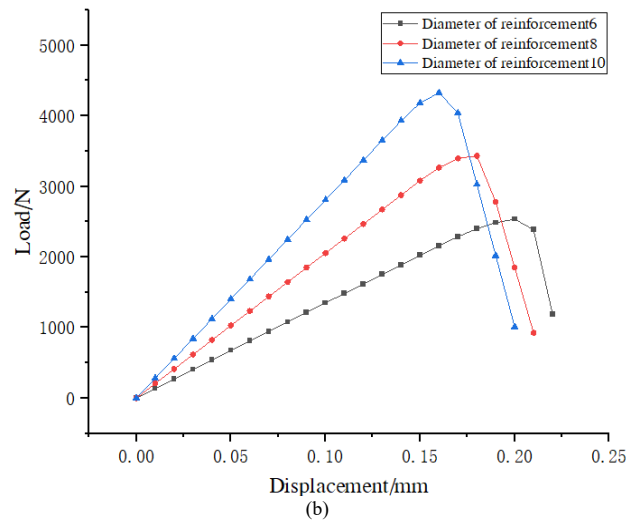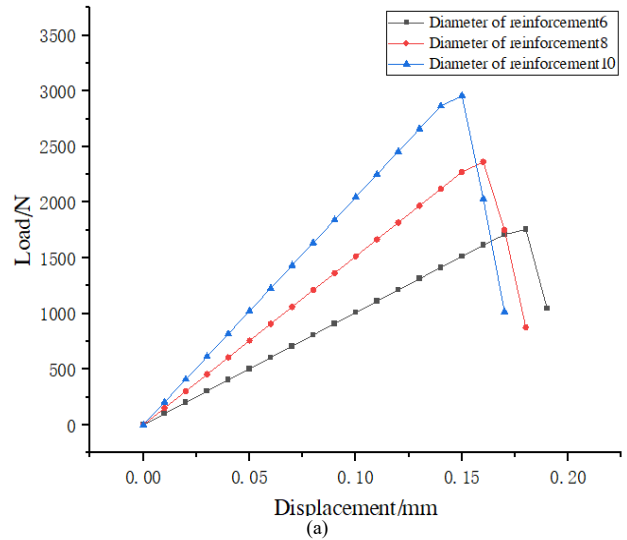

Fig. 11. Influence of different anchorage lengths on pullout force.

The simulation results show that when the anchorage length is 100, 150, 200, and 250 mm, the corresponding limit pulling forces are 1757.61, 2535.78, 3204.05, and 3759.93 N, respectively, in the 6 mm steel bar; 2362.07, 3434.44, 4376.19, and 5206.76 N, respectively, in the 8 mm steel bar; and 2957.22, 4328.66, 5571.91, and 6670.00 N, respectively, in the 10 mm steel bar. The point diagram of ultimate pulling force–anchorage length indicates that the ultimate force increases obviously with the increase in anchorage length, but it does not increase in a straight line, which accords with the general law of anchor reinforcement. For example, when the diameter of the steel bar is 10 mm, from the anchorage length of 100 mm to 250 mm, the limit pullout force changes are 1371.44, 1243.25, and 1002.43 N.

4.4 Relationship between ultimate pullout force and rockbolt diameter

This study considers three types of steel bars (rockbolt) with diameters of 6, 8, and 10 mm and four anchorage lengths of 100, 150, 200, and 250 mm. The relationship between pulling force and steel bar diameter is studied. The pulling force displacement diagrams of the three steel bar diameters at the four anchorage lengths are shown in Fig. 12.
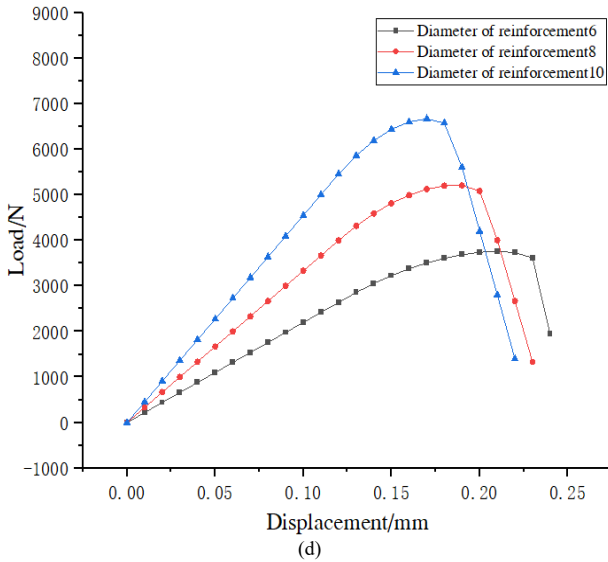
(d)

Fig. 12. Pullout force–displacement diagram for different anchorage lengths. (a) 100 mm. (b) 150 mm. (c) 200 mm. (d) 250 mm.

With the influence of steel bar diameter considered, the simulation results of the ultimate tensile force with the change in steel bar diameter are shown in Table 6.

As shown in Fig. 13, the larger the diameter of the steel bar, the greater the drawing force borne by the microanchor rod, and the shorter the pulling displacement required to reach the maximum stress. After the maximum drawing force is reached, the drawing force begins to drop sharply within a very short time, then the interface bonding fails completely. The simulation results show that under the condition of the same anchorage length of 100 mm, the drawing forces of the bars with diameters of 6, 8, and 10 mm reach their peak values at 0.18, 0.16, and 0.15 mm, respectively, and the corresponding ultimate drawing forces are 1757.61, 2362.07, and 2957.22 N, respectively. Under the condition of the anchorage length of 150 mm, the drawing forces of the bars with diameters of 6, 8, and 10 mm reach their peak values at 0.20, 0.18, and 0.16 mm, respectively, and the corresponding ultimate drawing forces are 2535.78, 3434.44, and 4328.66 N, respectively. Under the condition of the anchorage length of 200 mm, the drawing forces of the bars with diameters of 6, 8, and 10 mm reach their peak values at 0.21, 0.19, and 0.17 mm, respectively, and the corresponding ultimate drawing forces are 3204.05, 4376.19, and 5571.91 N, respectively.

Under the condition of the anchorage length of 250 mm, the drawing force of the bars with diameters of 6, 8, and 10 mm reaches the peak value at 0.21, 0.19, and 0.17 mm, respectively, and the corresponding ultimate drawing force is 3759.93, 5206.76, and 6670.00 N, respectively. Under the same anchorage length, the contact area between cement mortar and reinforcement diameter and the ultimate pulling force of the anchor rod increase with the increase in reinforcement diameter.

Table 6. Simulation results with the influence of rockbolt diameter considered.

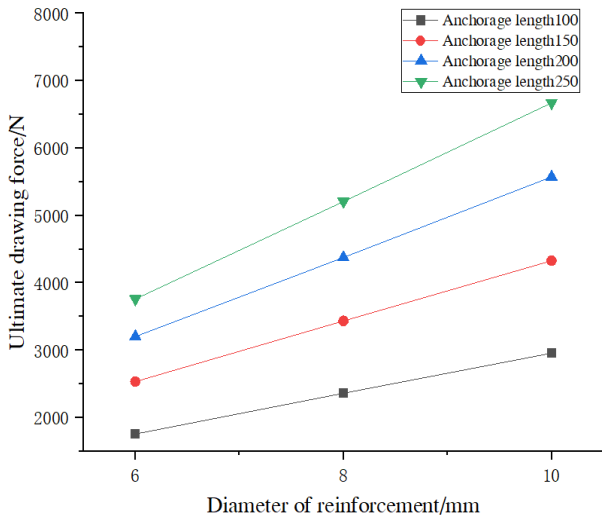| Rockbolt diameters (mm)	Ultimate pullout force (N)			
	Anchorage length 100 mm	Anchorage length 150 mm	Anchorage length 200 mm	Anchorage length 250 mm
6	1757.61	2535.78	3204.05	3759.93
8	2362.07	3434.44	4376.19	5206.76
10	2957.22	4328.66	5571.91	6670.00

Fig. 13. Effect of steel bar diameter on ultimate pullout force

4.5 Study on the ultimate pullout force and interface bonding strength of microrockbolt
The data directly obtained in the simulation process are the drawing force, and the bonding strength is calculated in accordance with the following formula [24]:

$$\bar{\tau} = \frac{F}{\pi D L} \quad (8)$$

where $\bar{\tau}$ is the average interfacial bonding strength (MPa), P is the ultimate pulling force of the bolt (N), L is the length of the anchorage section (mm), and D is the bolt diameter (mm).

The calculation results of interface bonding strength are shown in Table 7.

As the anchorage length increases, the ultimate tensile force increases. For example, when the diameter of the steel bar is 10 mm, the average bonding strength of the interface corresponding to the anchorage lengths of 100, 150, 200, and 250 mm is 0.941, 0.919, 0.887, and 0.849 MPa, respectively. The strength changes are 0.022, 0.032, and 0.038 MPa, with a decrease of 2.34%, 3.48%, and 4.28%, respectively. As the anchorage length increases, the bonding strength decreases. From the theoretical formula analysis, the ultimate tensile force and interface contact area increase, but the bonding strength decreases. That is, the increase in contact area is greater than the increase in ultimate tensile force, and the decrease has been increasing in the range of 100 mm to 250 mm. This result means that an increase in the anchorage length of this interval can effectively improve the anchoring effect at the interface between steel bars and cement mortar; the larger the anchorage length, the better the anchoring effect.

Table 7. Data of ultimate pullout force and average interfacial bonding strength.

Steel bar diameters	Anchorage length	Ultimate pullout force	Average interfacial bonding strength

| (mm)	(mm)	(N)	(MPa)
6	100	1757.61	0.932
	150	2535.78	0.897
	200	3204.05	0.850
	250	3759.93	0.798
8	100	2362.07	0.940
	150	3434.44	0.911
	200	4376.19	0.871
	250	5206.76	0.829
10	100	2957.22	0.941
	150	4328.66	0.919
	200	5571.91	0.887
	250	6670.00	0.849

Fig. 14. Ultimate tensile force and average interfacial bonding strength under different anchorage lengths and steel bar diameters. (a) 6 mm. (b) 8 mm. (c) 10 mm.

5. Conclusions

On the basis of the finite element analysis of the pullout process of microrockbolt–cement mortar, the axial stress distribution under monotonic load and the relationship between the ultimate pullout force and the interface bonding strength under different anchoring conditions were studied in this work. The following conclusions can be drawn:

(1) According to the simulation results, the failure mode of all models is bolt pulling out failure, that is, the interface bonding performance between the steel bar and the cement mortar fails, but the cement mortar is not damaged.

(2) With the increase in anchorage length and reinforcement diameter, the axial stress in the anchoring section decreases gradually and almost uniformly along the anchorage length.

(3) With the increase in steel bar diameter, the ultimate pulling force of the microbolt increases. The increase in anchorage length also causes the ultimate pulling force of the microbolt to increase, but the increase rate decreases.

(4) With the increase in the anchorage length, the ultimate pulling force increases, but the average interface bond strength decreases, specifically when the anchorage length is 100–250 mm. Therefore, within a certain anchorage length, the larger the anchorage length is, the more the anchoring effect of the microbolt can be effectively improved.

The disadvantage of this study is that it does not consider the influence of different grouting materials, bolt materials, and bolt surface morphologies on the ultimate tensile force and interface bond strength. In the next step, the two methods of laboratory test and numerical simulation will be used to compare laboratory test data with numerical simulation test data to study the influences of drilling diameter and other factors on the ultimate drawing force. A reasonable theoretical method applicable to the surface peeling disease of stone cultural relics is studied by the whole modeling of the three factors, which provides a reference value for practical engineering.

_____
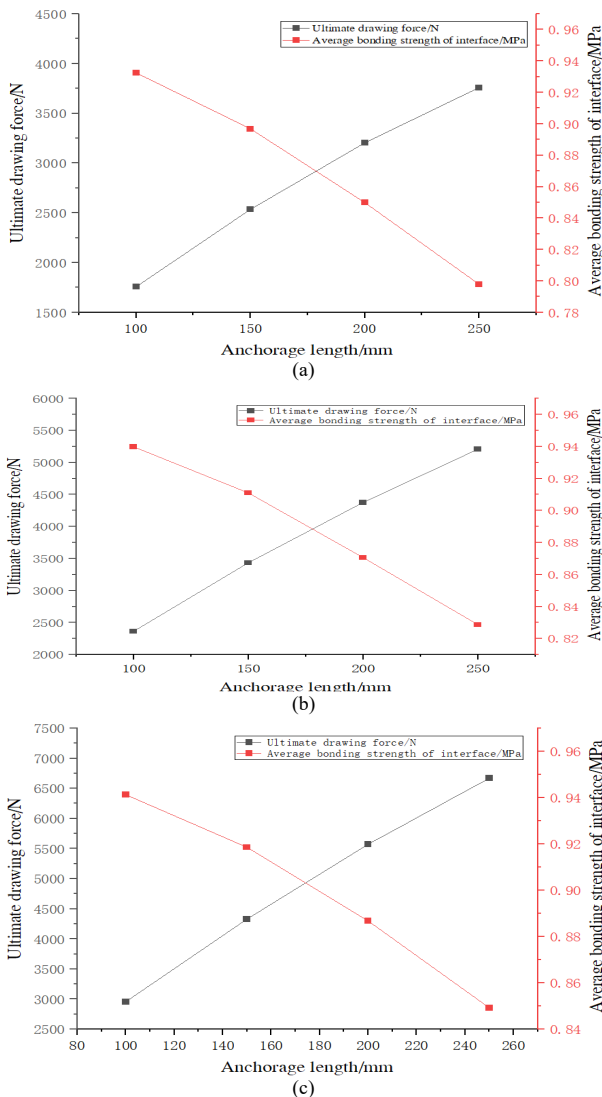
References

[1] H. Li, "Reflections and Exploration on the Construction of the Discipline of Cultural Relics Protection," *Stud. Natur. Cult. Herit.*, vol. 8, no. 1, pp. 37-51, Feb. 2023.

[2] Z. Wei, J. Chen, J. Qu, Q. Li, B. Zhang, and L. Wang, "Survey of Immovable Stone Cultural Relics and Analysis of Influencing Factors: A Case Study of the Qinglin Cave Statue in Feilaifeng, Hangzhou," *Stone*, no. 1, pp. 24-32, Jan. 2019.

[3] X. Chai, C. He, X. Li, and Q. Lu, "Influence of surface morphology of micro wood anchor reinforced by spalling disease in sandstone grottoes on resistance to pulling force," *Sci. Tech. Eng.*, vol. 16, no. 36, pp. 228-230, Dec. 2016.

[4] M. Zhao, S. Yan, K. He, Y. Dou, Y. Fang, and G. Zhai, "Experimental study on new materials for anti-seepage grouting of cracks in Longmen Grottoes, " *J. Changjiang River Sci. Res. Inst.*, vol. 33, no. 6, pp. 115-123, Jun. 2016.

[5] H. Lan et al., "Research progress on deterioration mechanism and instability mechanism of rock mass in Grottoes Temple," *Earth Sci.*, vol. 48, no. 4, pp. 1603-1633, Aug. 2022.

[6] H. Li, "Cultural relics rock material degradation shape classification research and application," *Sci. Conser. Archaeol.*, vol. 23, no. 1, pp. 1-6, Feb. 2011.

[7] J. Yu, B. Zhang, P. Shao, and B. Feng, "Cave temples and stone carvings of zhejiang province class cultural relics health assessment research review, " *Stone*, no. 3, pp. 29-36, Mar. 2018.

[8] J. Huang, J. Wang, F. Gao, F. Wang, Y. Qi, and S. Liu, "New progress in the protection of sandstone grottoes: A case study of Yungang Grottoes," *Southeast Cult.*, no. 1, pp. 15-19, Feb. 2018.

[9] J. Wang and J. Chen, "Analysis on the protection status and development of cave temples in China," *Southeast Cult.*, no. 1, pp. 6-14, Feb. 2018.

[10] J. Wang and X. Huo, "Discussion on key scientific issues and key technologies of cave temple protection," *Southeast Cult.*, no. 1, pp. 6-13, Feb. 2021.

[11] J. Wang, J. Chen, L. Wang, Y. Wang, and P. Gao, "Study on diseases and types of cave temples in China," *Southeast Cult.*, no. 4, pp. 25-32, Aug. 2022.

[12] S. Wang, H. Xiao, Z. Zou, C. Cao, Y. H. Wang, and Z. L. Wang, "Mechanical performances of transverse rib bar during pull-out test," *Int. J. Appl. Mech.*, vol. 11, Jun. 2019, Art. no. 1950048.

[13] S. Wang, C. Li, Z. Liu, and J. Fang, "Optimization of construction scheme and supporting technology for HJS soft rock tunnel," *Int. J. Min. Sci. Tech.*, vol. 24, no. 6, pp. 847-852, Dec. 2014.

[14] S.Wang, H. Xiao, P. Hagan, and Z. Zou, "Mechanical behavior of fully-grouted bolt in jointed rocks subjected to double shear tests," *DYNA*, vol. 92, no. 3, pp. 314-320, May 2017.

[15] Q. Fu, H. Huo, Y. Sun, F. Cheng, and J. Gao, "Numerical simulation of influence of bolt parameters on prestressed rock anchor foundation," *Wind Energy*, no. 10, pp. 60-64, Oct. 2018.

[16] R. Giot, C. Auvray, S. Raude, and A. Giraud, "Experimental and numerical analysis of in situ pull-out tests on rockbolts in claystones," *Eur. J. Env. Civil Eng.*, vol. 25, no. 12, pp. 2277-2300, Jun. 2019.

[17] N. Vlachopoulos, D. Cruz, B. A. Tatone, A. Lisjak, O. K. Mahabadi, B. Forbes, et al. "The performance of axially loaded, fully grouted rockbolts based on pull-out experiments utilizing fiber optics technology and associated numerical modelling of such support elements," *Geotech. Geol. Eng.*, vol. 38, no. 7, pp. 1389-1407, Apr. 2020.

[18] E. Komurlu and S. Demir, "Investigation of a new drilling design for loading core specimens with triple holes to determine direct tensile strength values of rock materials," *Mater. Des. Process. Commun.*, vol. 3, no. 2, Art. no. e154, Feb. 2020.

[19] H. Kou, H. Jing, K. Xu, and H. Tian, "Numerical simulation of bonding properties of GFRP bolt-mortar considering interface damage based on segmented model," *J. Hebei Univ. Eng (Natur. Sci. Ed.)*, vol. 38, no. 3, pp. 30-36+54, Sept. 2021.

[20] Y. I. Dimitrienko, Y. V. Yurin, T. R. Gumirgaliev, and G. A. Krasnov, "Creep deformations of curvilinear anisotropic media: finite element modeling," *J. Phys. Conf. Ser.*, vol. 1990, no. 1, Art. no. 012016, Aug. 2021.

[21] A. H. Abdel-Rahman and M. F. Awad-Allah, "Verification of pull-out resistance of anchors in soil/rock formations using empirical and finite element methods," *Innov. Infrastr. Solut.*, vol. 7, no. 1, pp 1-12, Jan. 2022.

[22] P. Małkowski, X. Feng, Z. Niedbalski, and M. Żelichowski, "Laboratorial tests and numerical modeling of rockbolts bonded by different materials," *Rock Mech. Rock Eng.*, vol. 56, no. 4, pp. 2589-2606, Dec. 2022.

[23] B. Liu and D. Li, "Experimental fitting analysis and simulation of the bond slip relationship of anchor mortar," *J. Hefei Univ. Tech.(Natur. Sci.)*, vol. 32, no. 10, pp. 1510-1513, Oct. 2009.

[24] B. Liu, D. Li, Y. Fang, G. Jin, and N. Tian, "Experimental study on the bond slip relationship between bolt-mortar interface and failure process analysis," *Chin. J. Rock Mech. Eng.*, vol. 30, no. S1, pp. 2790-2797, May 2011.

[25] Y. Tan, C. Qin, and Y. Wang, "Analysis of the interface peeling mechanism of anchor rods based on bilinear constitutive model," *Sichuan Building Sci.*, vol. 43, no. 1, pp. 28-33, Feb. 2017.

[26] M. Z. Zhao, D. E. Lehman, and C. W. Roeder, "Modeling recommendations for RC and CFST sections in LS-Dyna including bond slip," *Eng. Struct.*, vol. 229, Art. no. 111612, Feb. 2021.

[27] Y. Li, S. Yin, and Y. Liu, "Bond slip constitutive relationship between FRP reinforcement and seawater concrete with coral aggregate interface," *Acta Mater. Compos. Sinica*, vol. 39, no. 8, pp. 3950-3964, Sept. 2021.

[28] C. Kong, T. Yang, M. Xiao, and Q. Yuan, "Numerical simulation of fully grouted rockbolts with or without faceplates based on the tri-linear bond-slip model," *Constr. Build. Mater.*, vol. 367, Art. no. 130288, Feb. 2023.

[29] T. Tamiru, S. Seid, D. Bogale, and B. Ashuro, "Damage modeling and failure analysis of glass fiber-reinforced composite cylindrical laminates using continuum damage mechanics," *J. Fail. Anal. Prev.*, vol. 23, no. 4, pp. 1527–1537, Jun. 2023.

[30] M. Abbas, B. Bary, and L. Jason, "A 3D mesoscopic frictional cohesive zone model for the steel-concrete interface," *Int. J. Mech. Sci.*, vol. 237, pp. 107819, Jan. 2023.

[31] Z. Chen and Q. Luo, "Numerical analysis of mechanical properties of glass fiber reinforced composite concrete beams considering interface bonding and sliding," *Ind. Constr.*, vol. 49, no. 9, pp. 64-69, Sept. 2019.

[32] W. Hu, R. Guo, and Y. Ren, "Calculation of bending capacity of concrete beams reinforced by fiber reinforced material mesh based on cohesiveness model," *Ind. Constr.*, vol. 52, no. 3, pp. 216-226, Mar. 2019.